16

High-Speed, High-Power, and High Responsivity Photodiode for Radio-Over-Fiber (ROF) Communication

J.-W. Shi, F.-M. Kuo and Y.-S. Wu
Department of Electrical Engineering, National Central University
Taiwan

1. Introduction

The tremendous increase in the required volume of wireless data-transmission has stimulated attention on ways to use the millimeter wave (MMW) bands above 60GHz (V-band) or above 100GHz (W-band) as the carrier frequency for the realization of systems with very high transmission data rates in excess of many gigabits-per-second [1,2]. Unfortunately, there is a large propagation loss of the MMW signal in the >W-band or V-band frequencies, whether in free space or in a coaxial cable. One promising solution to this problem is the radio-over-fiber (ROF) technique [1-3], where the MMW signal is distributed through a lossless optical fiber and then radiated over the last-mile to the user-end. High-speed, high responsivity, and high-power photodiodes (PD) serve as a key component in photonic MMW communication systems [1] for transducing the intense optical power to high-power MMW power. The saturation current-bandwidth product is thus a key parameter for evaluating the performance of high-power photodiodes (PD) for such applications, especially when the operating frequency is around 100GHz or higher. By increasing the saturation current of the PD, we can boost the injected optical power and further increase the maximum available MMW power. The burden imposed on the MMW power amplifier can thus be relaxed [4,5]. Recently, a research group at NTT reported excellent results for a 10Gb/s wireless link at 120GHz, achieved by using a high-power uni-traveling-carrier photodiode (UTC-PD) based photonic transmitter [1,2].

There are two approaches to improve the high-power performance of PDs. One is to distribute and uniform the photocurrents along the edge-coupled PDs to minimize the thermal problem [6] and space-charge screening effect [4,5] by improving the geometric structure of optical and electrical waveguides, such as, evanescently-coupled photodiode (ECPD) [7-9]; the other is to minimize the space-charge screening effect in the photo-absorption volume by changing the structure or material of epitaxial layers, such as UTC-PD [4,5], partially depleted absorber photodiode (PDP) [10], and separated-transport-recombination photodiode (STR-PD) [11]. In this chapter, we reviewed our recent works on InP and GaAs based high-power photodiodes, which can overcome the above-mentioned problems and achieve state-of-the-art output power without seriously sacrificing the

responsivity and speed performance.

2. Geometric Structure of High-power, High-responsivity, and High-speed Photodiode

2.1 Introduction

Figure 1 (a) and (b) shows the cross-sectional view of vertical-illuminated PDs (VPD) and WGPD, respectively. Compared with the structure of typical VPDs, the structure of the edge-coupled waveguide photodiode WGPD [4] has attracted a lot of attention due to its superior bandwidth-responsivity product performance [4]. In VPDs strcuture, the direction of carrier transport is parallel with the direction of incident photon and in order to shorten the carrier drift-time inside the absorption regime, we must decrease the absorption layer thickenss and the reponsivity performance will thus be sacrifieced for high-speed perfroamnce. On the other hand, in WGPD structure, the direction of carrier transport is perpicdular to the direction of incident photon and we can still use a thin absorption layer (<200nm) to absorb the edge-coupling photon completely by using a proper length of active waveguide, however, its maximum output photocurrent is seriously limited, due to the problem of saturation at the input-end of device [4]. Figure 2 shows the conceptual diagram of input-end-satutaion problem in WGPD. As can be seen, most of the incident photon will be absorbed near the input-end of WGPD and the high density of photo-generated carriers would thus saturate the device output power. There are two major trends being followed to improve the high-power performance of the WGPD. One is to distribute and make uniform the photocurrents by improving the structure of optical and electrical waveguides, such as research into the velocity matched distributed photodetector (VMDP) [12] and the other is evanescently-coupled photodiode (ECPD) [7-9]. As can be seen in Figure 2, the incident photon is launched to the bottom passive optical waveguide of ECPD and gradually coupled to the upper active absorption region. Becasue the gradually coupling process into the absorption regime, the distribution of photo-generated carriers thus becoems more uniform and the problem of input-end saturation in traditional WGPD can thus be minimized. Recently, several research groups have demonstrated the state-of-the-art performance of ECPDs with a short coupling length (~20μm) and partially depleted absorber [8,9]. However, the tolerance of the cleaved coupling length of such devices is very small (less than 5μm) and different coupling lengths have a serious effect on the responsivity performance [8]. This problem can be overcome by dry etching a deep trench to precisely define the waveguide length [13]. However, any roughness on the dry-etched

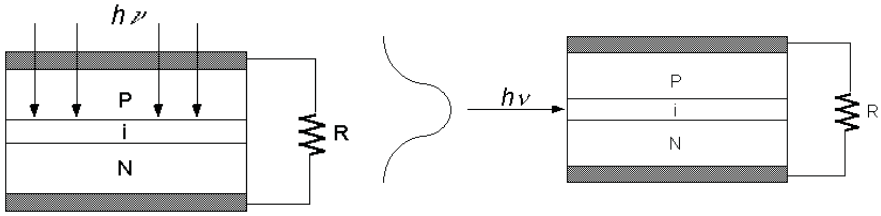

Fig. 1. Schematic diagram of a p-i-n based VPD (a) and WGPD (b) structure.

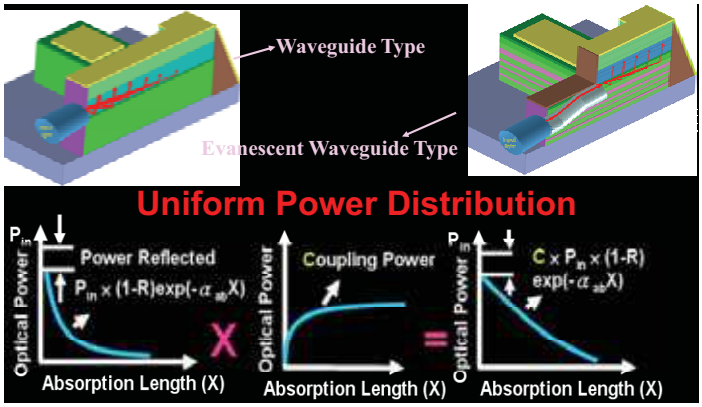

Fig. 2. The conceptual diagram of launched optical wave in the input-end of WGPD structure and ECPD structure

facets can degrade the responsivity performance. Other groups have also developed photodiodes with an asymmetric twin waveguide (tapered) structure to improve the cleaving tolerance and achieve high responsivity performance [7] but the misalignment between these twin waveguides and the optical scattering loss, which is induced by very long waveguide lengths (>700μm), can both seriously affect the responsivity [7]. In additiom, by integrating an edge-coupled PD with a leaky optical waveguide, is another possible soulution to increase the tolerance of the cleaving process [12], although the electrical bandwidth performance may be sacrificed for the high responsivity performance, due to the fact that a much larger photo-absorption volume than that of the traditional WGPD is necessary to completely absorb the diluted optical power [4,12]. In this chapter, we reviewed our recent works [14,15], which can overcome the abvoe-mentioned problems of ECPD and achieve the goal of high-bandwdith, high-responsivity, and high saturation power. At first, we combined a partially p-doped photo-absorption layer with a leaky optical waveguide and a distributed-bragg-reflector (DBR) in the structure of an edge-coupled photodiode. The integrated DBR mirror can fold the injected optical path and enhance the responsivity performance without increasing the device-absorption-length. The demonstrated device can achieve superior performance in terms of bandwidth, saturation power, and quantum efficiency for the control, without DBR mirrors. Furthermore, the responsivity performance of our demonstrated device is much less sensitive to the cleaved coupling length than is that that of the ECPD (7% vs. 30% [8]). The another structure we demonstarted for solving the problems of ECPD is the dual-step evanescently-coupled waveguide photodiode [15] (DECPD). By separating the fiber-guide region and coupling-guide region into different parts of the optical waveguide [15], the dependence of the responsivity on the cleaved-length can be minimized, nor is a long (~700μm) passive waveguide with complex tapered stages any longer necessary.

2.2 Leaky-Waveguide PDs

In order to determine the influence of DBR mirrors on the responsivity performance of photodiodes, two kinds of device, with the same geometry and epi-layer structures, but with and without DBR mirrors, were fabricated. The DBR mirror device has twice the reflected input optical power and absorption of the folded optical power. Thus, compared with the DBR device, the control device requires a much longer device-absorption-length, which results in poorer speed performance. The cross-sectional view and top-view of the demonstrated devices are given in Figure 3 and the inset shows the fabricated DBR mirror.

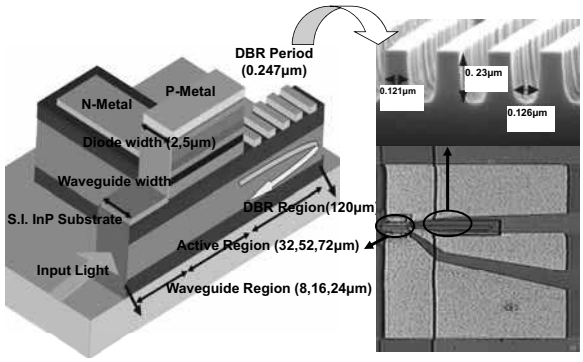

Fig. 3. The cross-sectional and top views of the demonstrated devices. The inset pictures the fabricated DBR mirrors.

The DBR mirror pairs (500 pairs), as labeled in Figure 3, are designed to produce a reflection maximum at around the 1550nm wavelength regime. The leaky optical waveguide used was composed of two lower undoped InGaAsP core layers, a thin heavily doped n-type InP etching stop layer, an $In_{0.53}Ga_{0.47}As$ based photo-absorption layer, 0.3μm undoped and 0.2μm p-doped in thickness, and a topmost p-type InP cladding

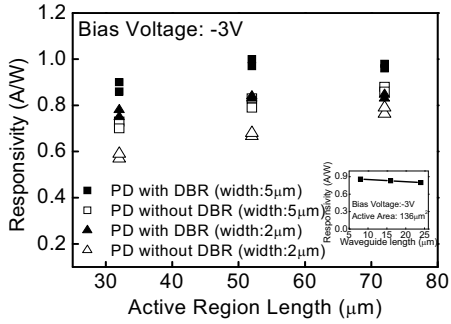

Fig. 4. The measured responsivity of both devices (with and without DBR mirrors) versus length of active diodes. The bias voltage is fixed at -3V and the waveguide widths of both

devices are 2μm and 5μm. The inset shows the measured responsivities of DBR devices with the same active area (136μm²) and different cleaved lengths of passive optical waveguide.

structure, without DBR mirrors, is around 200μm, and the theoretical calculated RC-limited bandwidth is just around 10GHz, in the case of a 50Ωload. By the incorporation of highly reflective DBR mirrors into our optical leaky waveguide, the required absorption-length can be shorten, meaning a superior bandwidth-responsivity performance product. The partially p-doped photo-absorption layer, shortens the thickness of the depletion layer and significantly increases the saturation current of the PD [10]. Figure 4 shows the measured maximum responsivity of both devices vs. the active diode lengths with different waveguide widths (2μm and 5μm). We can clearly see that all devices with DBR mirrors and different waveguide widths exhibit a much higher responsivity than that of the control device without DBR. The inset shows the measured responsivity of the DBR device vs. the cleaved waveguide length. We can clearly see that the measured responsivity is almost independent of the cleaved length. In comparison with the reported ECPD results, the measured responsivity will vary much more significantly (from ~0.7A/W to ~1A/W) when the cleaved length increases from 10μm to 20μm [7]. As shown in this figure, for a device with a DBR mirror, the achieved responsivity can be as high as 0.9A/W. Furthermore, our demonstrated device does not exhibit serious wavelength selectivity, which is a serious problem for the resonant-cavity-enhanced PD (RCEPD) [12]. This is because our cavity length is much longer than the operating wavelength and that an AR coating is applied to the input facet. The bandwidth and saturation current were measured with a heterodyne beating system. The traces shown in figure 5 (a) were from devices with and without DBR mirrors, with different active areas (96μm² and 136μm²) and almost similar responsivity performance (0.8 vs. 0.7A/W). Both devices were measured under the same dc bias voltage (-3V) and output photocurrent (5mA). Compared with the control, the device with DBR mirrors not only has higher electrical bandwidth performance (~40GHz vs. ~30GHz) but also produces higher bandwidth-responsivity (~32GHz-A/W vs. ~21GHz-A/W). Figure 5 (b) shows the measured frequency responses of devices with DBR mirrors and different active areas (96μm² and 160μm²) under a -3V bias voltage and a fixed 15mA output photocurrent. Even under such a high output photocurrent (15mA), both devices achieved

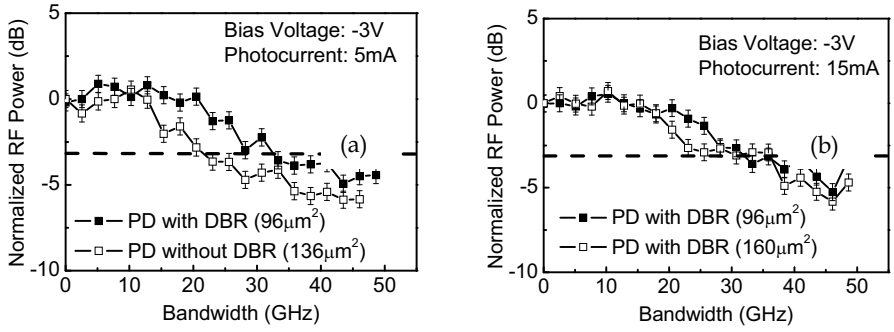

Fig. 5. (a) The measured frequency responses of devices under a fixed dc bias voltage (-3V) and output photocurrent (5mA). The active area of the devices, with and without DBR, is

96μm² and 136 μm², respectively. (b) The measured frequency responses of devices with DBR mirrors and two different active areas (96μm² and 160 μm²) under a fixed output photocurrent (15mA) and dc bias voltage (-3V).

an electrical bandwidth of around 40GHz. The high responsivity (0.8A/W and 0.9A/W) and high electrical bandwidth (~40GHz) that the demonstrated devices achieved under high current operation ensure their suitability for application to 40Gbit/sec analog and digital fiber communication systems. As compared to the results shown in Figure 5, we can clearly see that although the DBR device has larger active area than those of the control device (160μm² vs. 136μm²), the electrical bandwidth performance is still much better (~40GHz vs. ~30GHz) even under a much higher output photocurrent (15mA vs. 5mA). The superior high-power performance of the DBR device to the control device can possibly be attributed to its more uniform distribution of photo-generated carriers, because of the folded photo-absorption process. Figure 6 represents the photo-generated RF power versus dc photocurrent of devices under a fixed dc bias voltage (-3V). The ideal relation between the RF power of a 100% modulated large-signal and the average current with a 50Ω load is also plotted as a straight line for reference. As shown in this figure, DBR devices with a smaller geometric size (96μm² vs. 160μm²) can have a slightly larger photo-generated RF power under the same photocurrent, due to having a larger RC limited bandwidth. Furthermore, we can clearly see that the two DBR devices have a higher saturation current (~18mA vs. ~15mA) and RF power (6.4dBm vs. 2dBm) than that of the control devices with a 136μm² active area, due to their superior high power performance as discussed in Figure 3 and 4. The values achieved for RF power (6.4dBm), saturation photocurrent (~18mA), responsivity (0.8A/W), and electrical bandwidth (~40GHz) are comparable with the ECPD with PDP structure [16].

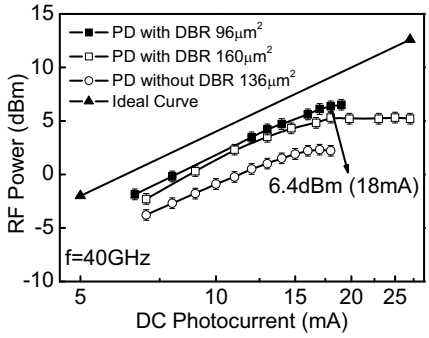

Fig. 6. The RF power versus dc photocurrent of both devices (with and without DBR) with three different active areas (squares: 96μm², open squares: 160μm², open circles: 136μm²) under a fixed 40GHz operating frequency and dc bias voltage (-3V).

2.3 Dual-Step Evanescently-Coupled Uni-Traveling-Carrier Photodiodes

A cross-sectional schematic diagram and the top view of the demonstrated DECPD are shown in Figures 7(a) and (b), respectively. Figure 7(c) shows a top view of the DECPD after zooming in on

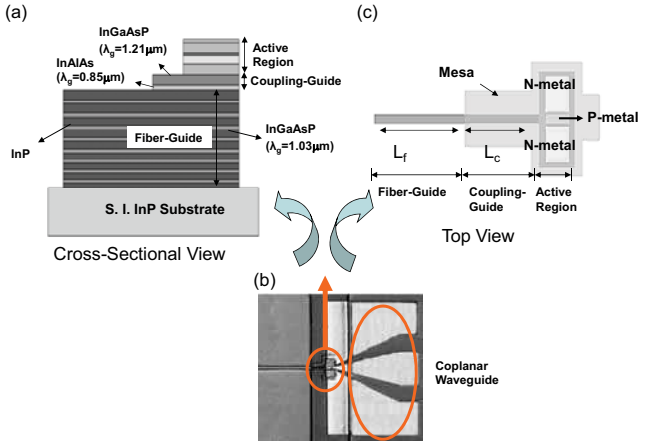

Fig. 7. (a) Cross-sectional view and (b) top-view of the demonstrated DECPD; (c) shows the top-view after zooming in on the active part of device. T and λ_g represents the thickness and bandgap wavelength of the specified epi-layer, respectively.

its active region. As shown in Figure 7(a), the first step in the bottom of our ECPD is a single-mode fiber-guide while the second step is the coupling-guide region. The lengths (L_f and L_c) of these two regions are marked in Figure 7(c). The fiber-guide is composed of nine InGaAsP layers, whose thicknesses increase from 100nm (bottom) to 314nm (top), in increments of 30nm, interspersed between the 80-nm-thick InP layers. In order to achieve low polarization dependence, low coupling loss, and maintain single-mode propagation, (which can benefit integration with other active or passive components in the planar-lightwave-circuit [17]), the index difference and thickness between InGaAsP and InP layers and the width (~5μm) and depth (~3μm) of the cross-section of our fiber-guide are all optimized using commercial three-dimensional (3-D) beam propagation method software (BPM). The insets to Figure 8 show the simulated mode spectrum and mode profile of light that propagates in the single-mode fiber-guide. Obviously, there is one significant dominant peak, of nearly 89% of the total input power, in this inset, which indicates that our fiber-guide can only support one mode (single-mode) propagation. We can thus understand that as the injected light couples into the upper coupling-guide region, it is always transferred with the same optical mode shape, regardless of the value of L_f, which is determined by the cleaving process. The second step in our passive waveguide is the coupling-guide region, which is composed of two n-doped InGaAsP ($1\times10^{18}cm^{-3}$) optical matching layers [8,9], for optical power coupling to the absorption region and good n-type ohmic contacts. The length of this coupling region L_c is precisely defined by the mask design rather than by the cleaving process. We can thus optimize L_c to achieve complete optical absorption for different active areas (lengths). Figure 8 shows the simulated optical

power distributions in our demonstrated devices. The simulated two DECPDs have the same active areas (76μm²) and active lengths (20μm), but different L_c (20μm and 35μm). The values of L_f obtained during the simulation are both around 300μm.

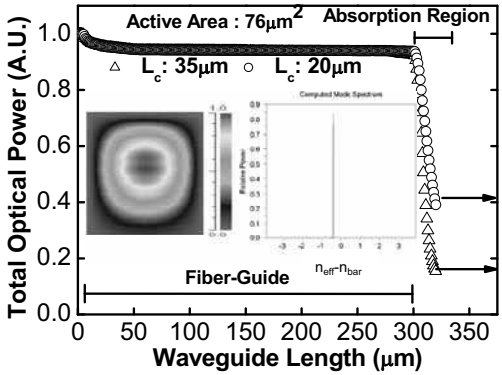

Fig. 8. Simulated optical power distributions without considering the optical scattering loss for devices with different coupling lengths and a fixed active area (76μm²). Triangle: L_c=35μm; circle: L_c=20μm. The arrowheads indicate the residual optical power after propagation through the active length (20μm). The insets show simulated cross-sectional views of the optical mode and mode spectrum in the fiber-guide region.

We can clearly see that by optimizing the value of L_c to be 35μm, the injected optical power for the active area (length) can be absorbed completely. The optimized values of L_c for devices with three different active areas; 56μm², 76μm², and 116μm², and a fixed waveguide width 2μm, are 40μm, 35μm, and 25μm, respectively. The active absorption region of our device has a typical UTC-PD structure [5]. The abrupt graded p-type doping profile ($2.5\times10^{17}\,cm^{-3}$ to $3\times10^{18}\,cm^{-3}$) in the absorption region is expected to minimize the speedy degradation phenomenon of our UTC-PD, especially when operating under a low output photocurrent [5]. Figure 9 shows the measured responsivity of our devices under a fixed bias voltage -3V and different polarization states versus different fiber-guide (cleaved) lengths L_f. The L_c of all the measured devices is fixed at 40μm. We can clearly see that the responsivity decreases as L_f increases, which may be attributed to the increase of optical scattering loss with L_f. The measured responsivity of our devices, which have the same 76μm² (56μm²) active area and different fiber-guide lengths (from 20μm to 50μm), is as high as around 1A/W (0.9A/W). The responsivity of the reported ECPD will oscillate seriously with the cleaved length (from ~0.7A/W to ~1A/W for cleaved lengths varying in the same range, 20μm to 50μm) [8,9]. We can thus conclude that, not only does our device demonstrate device high responsivity (~1A/W), but the cleaving tolerance is much higher (~around 50μm) than that of reported planar multi-mode ECPDs [8,9].

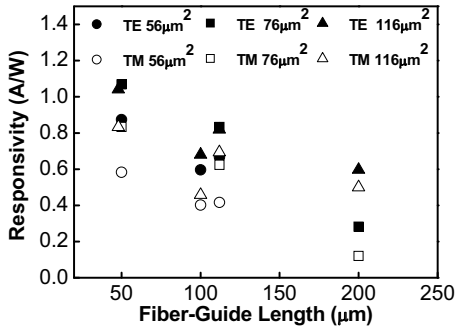

Fig. 9. Measured responsivity versus different L_f for devices with different active areas under a fixed bias voltage -3V.

The bandwidth and saturation current are measured with a heterodyne beating system. Figure 10 shows the measured frequency responses of the DECPD with different active areas under a fixed -1V bias voltage and a fixed photocurrent 5mA. The achieved 3-dB bandwidths of devices with actives areas of 56μm², 76μm², and 116μm² are around 60GHz, 50GHz, and 40GHz, respectively. The inset to Figure 10 shows the measured frequency responses of a device with an 116μm² active area under different reverse bias voltages and a small output photocurrent (0.5mA). We can clearly see that the speed performance of device is not degraded, even given such a small output photocurrent density (0.43kA/cm²) and different bias voltages. The past results reported for UTC-PDs indicate that they usually exhibit degradation of speed performance under low output photocurrent [5,18], which is an issue for high-speed fiber communication system [19]. The abrupt graded p-type doping profile in the absorption region of our device means that the static built-in electric field (1.6 to 19kV/cm) is around the critical field for the overshoot-velocity of the electrons. This in turn means that a smaller self-

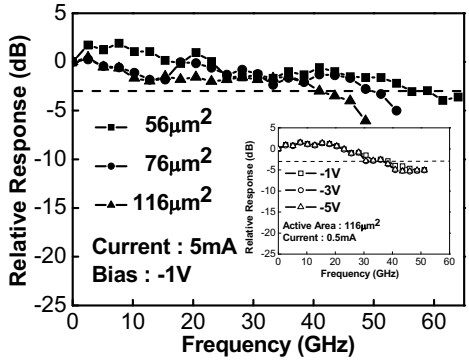

Fig. 10. Measured frequency responses of devices with different active areas under a fixed dc bias voltage (-1V) and a fixed output photocurrent (5mA). The inset shows the device

with an 116μm² active area measured under three different dc bias voltages (-1V, -3V, and -5V) and much lower output photocurrent (0.5mA)

induced field (photocurrent density) will be required to accelerate an electron to near its overshoot-velocity, thereby minimizing the problem of bandwidth degradation under low currents. Figure 11 shows the photo-generated RF power of the devices with (a) 56μm², and (b) 116μm² active areas. The three traces show the results measured under three different bias voltages (-1V, -2V, and -3V). The operating frequency is fixed at 60GHz and 40GHz for (a) and (b), respectively. The ideal relation between the RF power of a 100% modulated large-signal and the average current on a 50Ω load is also plotted as a straight line for reference. The maximum values of the RF power and dc photocurrent of the device with a 56μm² active area are limited by the thermal failure of the device. On the other hand, for a device with a larger active area (116μm²), significant saturation occurs at around 19mA photocurrent. The observed thermal-damage in our small device (56μm²) may be attributed to its larger electrical and thermal resistance, compared with that of a large device (116μm²). The values obtained for saturation current-bandwidth are around 780mA-GHz for both devices. In comparison with other reported high-performance ECPDs with a 25Ω effective load [20] or partially depleted absorbers (PDA)-ECPDs [16] with a 50Ω load, our demonstrated device can achieve a comparable bandwidth-responsivity (54GHz-A/W vs. 60GHz-A/W [20] and 40GHz-A/W [16]), and a higher saturation current-bandwidth performance (780mA-GHz vs. 520mA-GHz [20] and 680mA-GHz [16]).

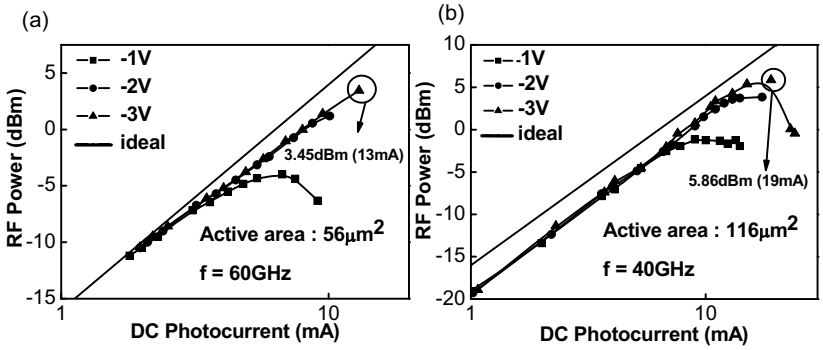

Fig. 11. The RF power versus dc photocurrent of both devices (with and without DBR) with three different active areas (squares: 96μm², open squares: 160μm², open circles: 136μm²) under a fixed 40GHz operating frequency and dc bias voltage (-3V).

3. Epitaxial Layer Structure of High-Power Photodiodes

3.1 Introduction

Ultra-high-speed and high-output-power performances are two main trends in the progress of all semiconductor-based devices for telecommunication. However, in most cases, speed and power performances are usually two-trade off parameters in the design of these devices, which include ultra-high speed PDs [4]. By properly down scaling the photo-

absorption volumes of PDs, ultra-high speed performances can be achieved, due to the reduction of parasitic capacitance and resistance in PDs. However, the small photo-absorption volume ($\sim 1\mu m^3$) would cause a high density of photo-generated free carriers and induce a strong space charge field that screens the external applied bias field. The electrical bandwidth would thus seriously degrade due to the reduction in drift velocity of photo-generated carriers [4,5]. There are two major ways to increase the output saturation current (power) and electrical bandwidth product performances, the one is to distribute the photocurrents along edge-coupled PDs, such as the velocity matched distributed photodetector (VMDP) [12] and ECPD as we discussed before, the other is to shorten the carrier drift-time in the active photo-absorption volume, such as UTC-PD [4,5] and seperated-transport-recombintaion PD (STR-PD) [11]. In this chapter, we will introduce the fundamental trade-off between speed and power of ultra-high speed PDs, review the previous reported ultra-high speed/power PDs, and also our recent work about PD with state-of-the-art saturation current-bandwidth product performance.

3.2 Space-Charge-Screening (SCS) Effect in Photodidoe

Field-screening is a fundamental mechanism that limits the output power and electrical bandwidth of PDs under high optical power illumination. A simple model illustrates physical phenomena that mitigate field-screening effects in high-speed PDs, as discussed below. Filed screening arises when the dipole due to spatial separation of photo-generated charges, significantly reduces the drift field. This is especially serious when the photo-generated hole resides in the photo-absorption volume, due to its low mobility and the existence of hetero-structure barriers in p-i-n PDs as illustrated in Figure 12.

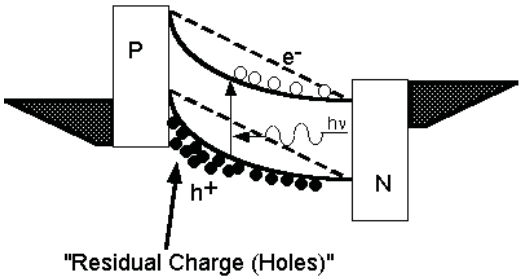

Fig. 12. The serious space-charge screening is originated from hole storage in photo-absorption volume.

The electric field in the photo-absorption layer is the sum of the built-in field (E_b), the field due to photo-generated free charges (E_f), and the fields of waves originating elsewhere and propagating inside the structure (E_w), $E = E_b + E_f + E_w$. The space charge field is found by Gauss's law and is proportional to the charge area density. For simplicity and clarity, the built-in field and the charge densities of the electrons and holes are approximated as rectangle functions in Figure 13. Figure 13 shows three sets of conceptual graphs at successive times after photo-generation of electrons and holes in the photo-absorption volume by a short optical pulse. The upper plot shows the photo-generated charge densities,

and the lower plots show the net electric field in the absorption region. Electron and hole velocities are assumed equal. The field resulting from the separation of the free charges opposes the built-in field, and if the charge density is large enough, may actually cancel it, as shown in the third set of graphs. Further, besides these, from the above figures, we can clearly see that the region with the least electric field is near the center of absorption region, where the carriers, especially for the case of hole, in the low-field region will travel slow, causing a slow component in the device photocurrent response. Field-screening is said to occur when the device response is perceptibly affected.

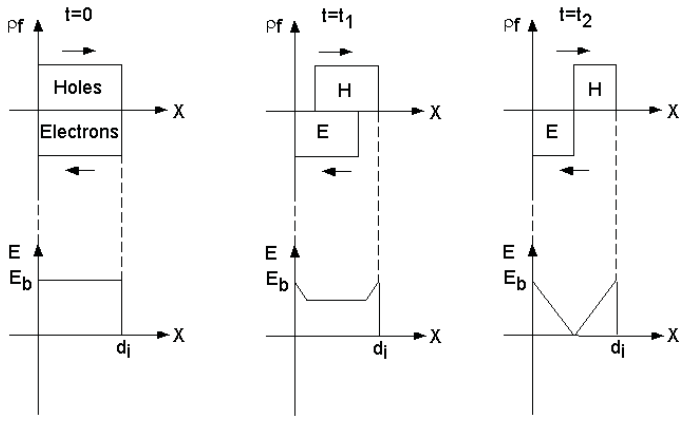

Fig. 13. Conceptual illustration of field-screening mechanism. Simplified electron and hole distributions and net electric fields in the depletion region are plotted at three times after photo-generation by a short optical pulse.

$$E_{eff} = \left(\frac{V_{bais} - Z_{load} \times J \times A + V_{bi}}{D} \right) - \left(\frac{J \times D}{V_{hole} \times \varepsilon} \right) \quad (1)$$

$$V_{hole} = V_{pl} \times \tanh\left(\frac{\mu_h \times E_{eff}}{V_{pl}} \right) \quad (2)$$

Symbol	Quantity & Value
E_{eff}	Effective electric field intensity (V/m)
V_{bais}	Applied voltage (V)
A	Active area of photodiode
J	Generated current density (A/m^2)
V_{bi}	Built-in voltage of diode (0.7 V)
D	Depletion layer thickness(m)
ε	Dielectric Constant of InGaAs ($1.23*10^{-10}$ F/m)
V_{hole}	Hole Velocity (m/s)
V_{pl}	Maximum Hole Velocity ($4.8*10^4$ m/s)
μ_h	Hole Mobility ($60\ cm^2/Vs$)
Z_{load}	Load Impedance (50Ω)

Table 1. Symbols and quantities for equation (1) & (2)

Eq. 1 and 2 is the transcendental equation for solving the net magnitude of electric field in the photo-absorption region and the drift velocity of photo-generated hole, respectively. The

physical meanings and values of each parameter are given in Table 1. We can clealrly see that in order to increae the E_{eff} and saturation current of photodode, we must reduce the depeletion layer thickness (D) or increase the carrier drift-velocity (V_{hole}). By increasing the drift-velocity of photo-generated carriers, such as with the structure of a UTC-PD, is one way to minimize the SCS effect. Excellent high-speed and high-power performance has been demonstrated [4,5] in UTC-PD. Figure 14 shows the conceptual band diagram of UTC-PD. Compared with the traditional p-i-n structure, the photo-absorption layer in the UTC-PD is a p-type doped epi layer instead of an intrinsic layer, thus the photo-generated holes will relax to the p contact metal directly without drift, diffusion or accumulation in photo-absorption layer, which will cause serious bandwidth degradation due to the space-charge screening effect. The photo-generated electrons in the absorption layer will diffuse into an intrinsic layer. In order to reduce the diffusion time of electrons in p-type layer, graded-doped or graded-bandgap absorption layers have been demonstrated in UTC-PDs [4,5] as in the n-p-n hetero-junction bipolar transistor (HBT) devices. Without the poor transport properties, such as low mobility and low drift velocity of the photo-generated holes, high power-bandwidth product performance of VPD type, WGPD type, and distributed type UTC-PDs have been demonstrated [4,5,21].

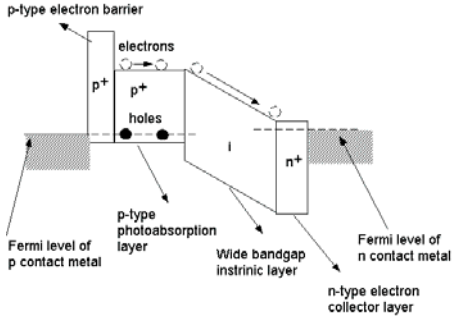

Fig. 14. The conceptual band diagram of UTC-PD

3.3 Near-Ballistic Uni-Traveling Carrier Photodidoe (NBUTC-PD)

The structure of UTC-PD, as discussed before, has attracted much attention due to its excellent speed and output power performance. However, such a device usually suffers from the problem of bandwidth degradation under high dc external bias voltage [4,5] due to both the high electric field existing at the junction of the collector (C) and photo-absorption (P) layer, and the decrease in the overshoot drift-velocity of photo-generated electrons. One possible way to enhance the speed performance of UTC-PD is to reduce the externally applied bias voltage and let the value of the electric field in the C-P junction approximately for the critical field, which will enhance the drift-velocity of photo-generated electrons [4,5]. However, under such low reverse bias voltage (around -1V for 200nm collector), the field-screening effect, which originates from the difference in polarity between the output ac voltage across the standard 50Ω load and the dc bias voltage, will seriously limit the maximum output photocurrent of the UTC-PD. Near-ballistic UTC-PD (NBUTC-PD) with state-of-the-art performance has been demonstarted to overcome the above-mentioned problems [22,23]. By inserting an additional delta-doped p^+ charge layer and an electric-

field-suffer layer into the collector layer, we can produce an appropriate value of electric field in most of the collector layers so as to sustain a peak velocity of photo-generated electrons under certain ranges of bias voltage and output photocurrent.
Figure 15 shows the conceptual band diagram of InP based NBUTC-PD. The major difference in the epi-layer structure between the UTC-PD and the demonstrated NBUTC-PD is the additional planar-doped p^+ $In_{0.52}Al_{0.48}As$ charge layer and the 100nm thick undoped $In_{0.52}Al_{0.48}As$ electric-field-suffered layer (E). The basic working principle of the NBUTC-PD is similar to that of the reported "Ballistic Collection Transistor (BCT)" [24], whose near-ballistic transport property has been verified through Monte Carlo simulations and experiments [25]. By introducing the proper planar doping density ($5\times10^{11}cm^{-2}$) into the depleted p^+ charge layer, the maximum electric field in the $In_{0.52}Al_{0.15}Ga_{0.33}As$ collector layer can be controlled to produce an appropriate value (around 40kV/cm at -5V bias) to sustain the overshoot velocity of the photo-generated electrons under a certain range of bias

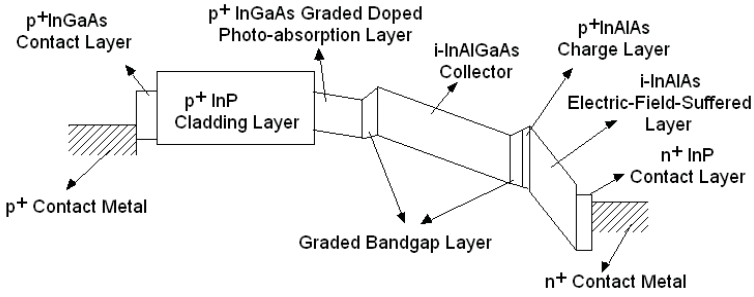

Fig. 15. The conceptual band diagram of NBUTC-PD

voltages and output photocurrents. The adopted graded p-type doping profile of the P layer can produce a built-in electric field (1.6 to 19kV/cm) around the critical field for the electron overshoot velocity. This means that a small self-induced field (photocurrent density) will be required to accelerate an electron to near its overshoot-velocity in the P layer [15]. Through this special P and C two-layer design, near-ballistic-transport of photo-generated electrons throughout the whole epi-layer structure can thus be expected. NBUTC-PDs with ECPD and back-side illuminated VPD structures [22,23] have both been demonstarted. Both kinds of strcuture have demonsatrted ecellent speed and power performance.
Figure 16 (a), (b) shows cross-sectional view and top views of the demonstrated NBTUC-PD with ECPD structure, respectively. The optical waveguide structure of our demonstrated NBUTC-PD is based on the reported high-performance planar evanescently-coupled photodiode as discussed before [8,9]. Extremely high responsivity of 1.01A/W and 1.02A/W was achieved with 150μm² and 200μm² active areas, respectively. The responsivity of the device with an 8μm waveguide/diode width and 40μm (320μm² active area) absorption length could be further improved to 1.14A/W. To our knowledge, these are the highest values ever reported for the responsivity of high-speed and high power UTC-PDs [4,5]. Figure 17 shows the typical frequency responses of the device with a 200μm² active area under different levels of the output photocurrent (0.5mA, 5mA, and 20mA) and a fixed dc bias voltages (-5V). One can clearly see that under 0.5 and 5mA operation, the electrical

bandwidth was around 40GHz. When the photocurrent reached 20mA, the bandwidth of device increased to 50GHz. Figure 18 shows the measured and fitted frequency responses of the device with a 320μm² active area under 10mA and 15mA

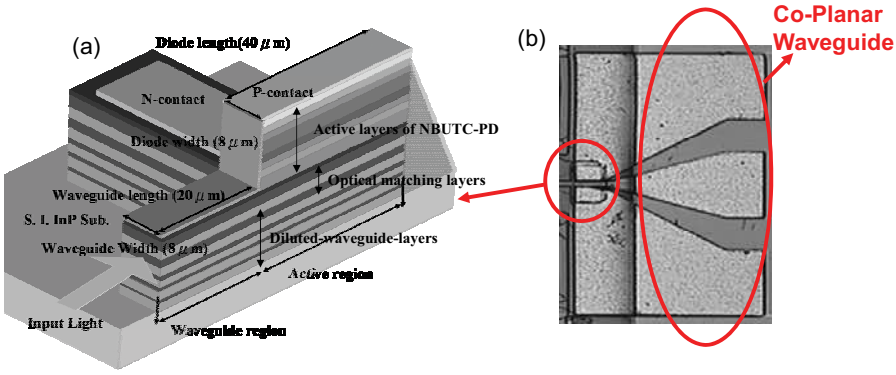

Fig. 16. Cross-sectional view (a) and top-view (b) of NBUTC-PD, which incorporates with an evanescently-coupled optical waveguide.

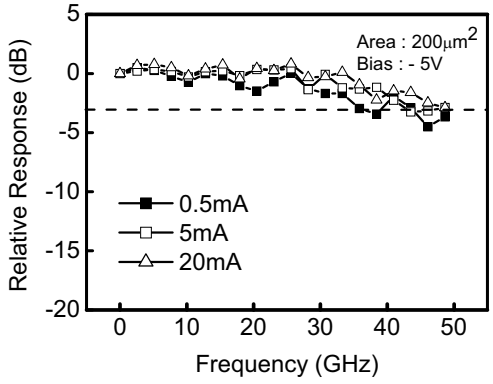

Fig. 17. The measured frequency responses of the device with a 200μm² active area under different levels of the output photocurrent and a fixed dc bias voltage (-5V). (square: 0.5mA; open square: 5mA; open triangular: 20mA).

output photocurrent values. The dc bias voltage was fixed at -4V. According to our simulation results, the bandwidth improvement under high current operation (15mA) is associated to the reduction of the transport time as discussed above and the ac capacitance [18]. The total capacitance is reduced due to the subtraction of the differential ac capacitance $I_C \times (d\tau_C / dV_{ac})$, proportional to the current, from the depletion capacitance [13,18]. Where, V_{ac} is the output ac voltage of device, I_C is the photocurrent, and τ_C is the

electron drift time. For the case of demonstrated device, such effect should be significant due to that under near-ballistic transport, the variation of drift-velocity (time) vs. the electric field (V_{ac}) is obvious, according to the reported field dependence electron drift velocity of III-V semiconductors. On the other hand, for the case of UTC-PD operated in the velocity-saturation regime, such effect can almost be neglected due to the fact that electron velocity is insensitive to the electric field. In our bandwidth simulation model, we thus used different

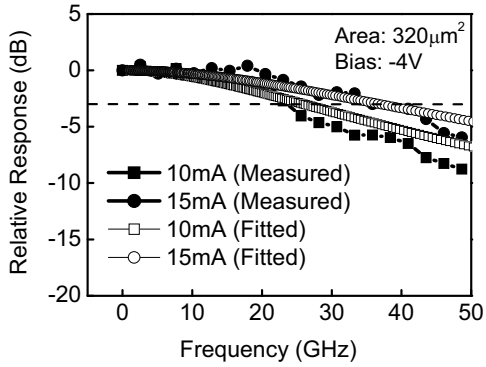

Fig. 18. The measured and fitted frequency responses of the device with a 320μm² active area under different output photocurrent values and a fixed dc bias voltage (-4V) (square: measured trace under 10mA operation; circle: measured trace under 15mA operation; open square: fitted trace under 10mA operation; open circle: fitted trace under 15mA operation.).

drift-velocities and the variation of slopes of electron drift-velocity vs. the electric field in $In_{0.53}Ga_{0.47}As$ material to roughly estimate the reduction of total capacitance and fit the measured frequency responses. Figure 19 shows the fitted and measured microwave S_{22} parameters of NBUTC-PD with a 320μm² active region for a broad frequency range (from 40 MHz to 50 GHz) under two different output photocurrents (1mA and 20mA) and a fixed bias voltage of -5V. The obvious difference between the S_{22} parameters under low and high photocurrents indicates the variation of the elements' values in the equivalent-circuit-model. Under high current operation (20mA), the traces of S_{22} in the Smith-Chart are closer to the S_{22} traces of the case of ideal open-circuit than the measured S_{22} trace under low current operation (1mA) are, which implies a significant improvement in the microwave characteristics of device. This phenomenon has never been observed before in the traditional p-i-n PD. The measured frequency responses of the S_{22} parameters of ordinary PDs or UTC-PD are usually insensitive to their output photocurrent [26]. As compared with the reported UTC-PD [4,5], NBUTC-PD can achieve almost the same electrical bandwidth (around 40GHz), even with a much larger device size (320μm² vs. ~120 μm²), and responsivity. This implies that the NBUTC-PD can achieve better output power and responsivity performance with a larger device size without sacrificing speed seriously due to the superior transport property of photo-generated electrons. The traces shown in Figure20 represent the photo-generated RF power vs. dc photocurrent of the NBUTC-PD under different bias voltages (-1V, -3V, and -5V).

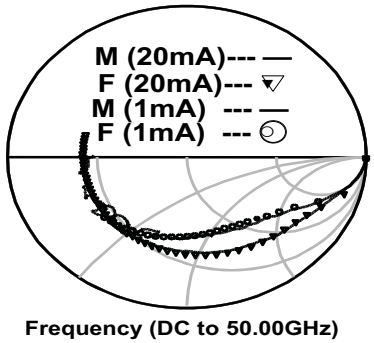

Fig. 19. The measured and the fitted S_{22} parameters of the device with a 320μm² active area under different levels of output photocurrent (1mA and 20mA) and a fixed dc bias voltage (-5V). The two solid lines represent the measured S_{22} under 1mA and 20mA. Traces with open circle and close triangle symbols represent the fitted results under 1mA and 20mA, respectively.

The operating frequency was fixed at 40GHz. The ideal relation between the RF power of a 100% modulated large-signal and the average current on a 50Ω load is also plotted as a straight line for reference. For the case of a –5V bias, the traces of the device with different active areas (200μm² and 320μm²) are also shown for the purpose of comparison. Since, the bandwidth of the device with a 320μm² active area increases as the photocurrent increases significantly under a -5V bias, the output RF power is closer to the ideal line than is the case with a low photocurrent.

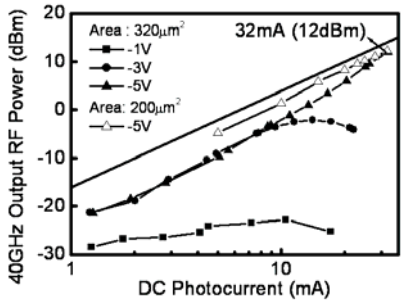

Fig. 20. RF power versus dc photocurrent of the devices with different active areas under different reverse bias voltages (square: -1V, circle: -3V, triangle (open triangle): -5V) at a 40GHz operating frequency. The ideal relation between the RF power and current on a 50Ω load is plotted as a straight line for reference purpose.

As compared to the structure of ECPD, the VPD structure may have further improved high-power performance due to that the input-end saturation problem can be eliminated. However, its responsivity may be poorer. Fortunately, when the operation frequency is over 100GHz, the maximum output saturation power from PD becomes a key isssue instead of efficiency due to that the over 100GHz MMW power amplifier still remains a challenge. The